Research Paper

# Wafter design for totally enclosed electric machines

Marco Satrústegui *, Gurutz Artetxe, Ibon Elosegui, Miguel Martinez-Iturralde, Juan C. Ramos

Ceit and Tecnun (University of Navarra), Paseo Mikeletegi 48, San Sebastian 20009, Spain

## HIGHLIGHTS

- Design criteria of wafters for totally enclosed electric machines.
- An experimentally validated CFD model for the modelling of electrical machines.
- Statistical models to predict the convective heat transfer in the end windings.
- The influence of wafters in the working temperatures of a particular machine.

## GRAPHICAL ABSTRACT
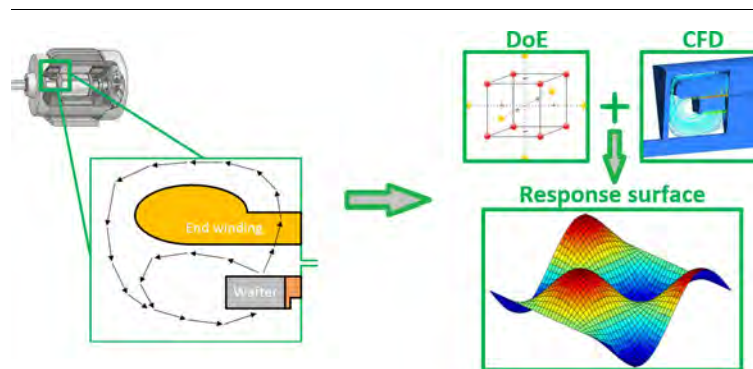


## ARTICLE INFO

## ABSTRACT

A computational fluid dynamics (CFD) model representing the effect of wafters in a totally enclosed electric machine is presented, introducing the most relevant theoretical assumptions and simplifications. The validation of the model is conducted through experimental measurements. From the CFD simulation data, a second-order response surface is developed using statistical tools, from which the wafters' influence on the convective heat transfer from the stator end windings is predicted. Wafter design criteria are obtained from the response surface information. Finally, a specific case is analysed, showing through CFD simulations that temperatures in the machine are reduced by including wafters in the design.

## 1. Introduction

Power density and rotation speed in electric machines have augmented significantly in recent years for many applications. This trend is resulting in an increase in losses for small volumes, and the cooling system is turning out to be a crucial aspect of the design. There are many options that provide very good cooling capabilities; liquid cooling through a jacket over the stator back iron is a widespread option [1–4], and direct oil-cooled systems provide very effective cooling throughout the machine [5,6], although it creates extra friction losses which could be very limiting as the rotation speed increases. Moreover, there are many combinations of both systems in the literature. For example, Equipmake Ltd. [7] proposed a dual cooling system that pushes oil through the slots and air through the rotor, Porsche [8] manufactured a 95 hp motor cooled with an oil jacket combined with an air induction system, and Lim in [9] developed an oil spray cooling system for in-wheel motors in electric vehicles.

This article focuses on totally enclosed cooling systems, which are widely used for traction applications, such as electric vehicles or trains [10]. This cooling arrangement shows significant limitations when it comes to rotor cooling [11], and the design also turns the end windings into a limiting factor, as they often become a

* Corresponding author.
  E-mail address: msatrustegui@ceit.es (M. Satrústegui).

**Nomenclature**

*Latin symbols*

| | |
|---|---|
| $b_{wafter}$ | width of the wafter |
| CCD | central composite design |
| CFD | computational fluid dynamics |
| $C_p$ | specific heat (J/kg K). |
| Cu | copper |
| $D_{Ext-Rotor}$ | rotor external diameter (mm) |
| $D_{Ext-Stator}$ | stator external diameter (mm) |
| DE | drive end |
| DoE | design of experiments |
| $D_{Shaft}$ | shaft diameter (mm) |
| f | factorial in the parametric study |
| GCI | grid convergence index |
| $h_{endwinding}$ | convective heat transfer coefficient in the stator end windings (W/m²·K) |
| $h_{tot}$ | mean total enthalpy |
| $h_{wafter}$ | height of the wafters (mm) |
| $l_{end-air}$ | distance between the end-plate and the end winding (mm) |
| $l_{endwinding}$ | axial length of the stator end winding (m) |
| $l_{Stack-Stator}$ | axial length of the stator stack (mm) |
| $l_{wafter}$ | axial length of the wafters (mm) |
| N | rotational speed (rpm) |
| NDE | non-drive end |
| n | Number of parameters in the parametric study |
| p | pressure (Pa) |
| $P_{Cu,s}$ | losses in the stator windings (W) |

| | |
|---|---|
| $P_{ventilation}$ | ventilation losses inside the machine (W). |
| $r_{ext}$ | external radius for the definition of the wafter height (mm) |
| $r_{int}$ | internal radius for the definition of the wafter height (mm) |
| $R^2$ | coefficient of determination of the statistical model |
| $R_{uu}$ | electrical resistance of the phase u of the stator winding (Ω) |
| $R_{vv}$ | electrical resistance of the phase v of the stator winding (Ω) |
| $R_{ww}$ | electrical resistance of the phase w of the stator winding (Ω) |
| $S_E$ | external energy source. |
| $S_M$ | external momentum source |
| t | time |
| T | Temperature of the fluid |
| $U_j$ | Flow velocity in direction j (m/s) |
| V | nominal voltage of the machine (Volts) |
| $X_{wh}$ | non-dimensional parameter that defines wafter height |
| $X_{wl}$ | non-dimensional parameter that defines wafter length |
| $z_{wafters}$ | number of wafters in the design |

*Latin symbols*

| | |
|---|---|
| μ | Dynamic viscosity (Pa·s) |
| ρ | Density of the fluid (kg/m³) |
| τ | Molecular stress tensor |

hotspot in the machine [12]. However, many solutions to these problems are available in the literature: Polikarpova [13] included potting to enhance the heat transfer from the end windings to the water jacket; Micallef [14] proposed the attachment of some wafters to the rotor in order to increase convective capacity in the end windings; Fedoseyev [15] removed the energy from the rotor through a heat pipe within the rotor shaft and transferred it to a heat sink; Tighe [16] provided a comprehensive thermal analysis of three different cooling configurations, including a heat pipe in the shaft to enhance heat transfer in the rotor. In addition, Camilleri in [17] conducted a CFD (computational fluid dynamics) parametric study of the effects of including radial vents in the rotor.

Of all these solutions, the inclusion of wafters solves the overheating in the end windings and maintains the simplicity of the cooling system. The primary purpose of including wafters is to increase the convective heat transfer coefficient in the stator end windings, which translates into a temperature reduction in this zone, which is usually very critical in traction applications. However, the lack of information about their design complicates their implementation in new designs.

Although Micallef [14,18,19] has studied accurate CFD models that represent the effect of wafters in the end space of a specific machine, there are still no established criteria for easily implementing wafters in a cooling system. This article, therefore, focuses on obtaining a design procedure and some design criteria for this element in order to maximize the convective heat transfer in the end windings and minimize the possible hotspots in this zone.

The proposed design methodology focuses on wound windings, which are the most extended winding topology for these kinds of applications. However, new trends in this field, such as hairpin [20] or coil-form windings [21], are gaining ground. Therefore, an independent study of each kind of topology should be carried out in further research.

The entire study has been conducted via CFD simulations. The CFD model used in this article has been previously validated with experimental measurements, and it has been employed along with statistical tools with the aim of generating a second-order response surface model that is capable of predicting the influence of different parameters that define the wafters on the convective heat transfer in the end windings of the machine. Thus, this paper presents an innovative approach to designing wafters for totally enclosed machines, with the aim of reducing the temperatures in the machine and increasing the overall efficiency of the system.

The CFD model employed in this study is described in detail first, including detailed information about its geometry and its mathematical model. Secondly, the validation process is analysed, including information about the experimental measurements obtained and a comparison between the tests and the CFD results. Then, the proposed parametric study is detailed, defining the type of study and the parameters included in the analysis. Finally, the results are summarized, giving the details of the second-order models for the convective heat transfer and the ventilation losses for both the machines with and without wafters. In addition, the effect of including wafters in a particular machine is reported, the result being a significant decrease in the temperatures of the machine.

## 2. CFD model

As the flow pattern in the end space is not predictable, it would be almost impossible to analytically determine the airflow in this zone. Therefore, a reliable CFD model which could accurately represent the effect of wafters in the end space of an electric machine is presented. The electric machine modelled is described in the next section.

The most relevant aspects of the geometry and the discretization are given first, followed by information about the mathematical model, explaining the main features of the CFD model itself.

## 2.1. Geometry

The CFD model represents the tailor-made machine shown in Fig. 1. It consists of a totally enclosed electric machine with an outer stator and an inner rotor without magnets or copper bars (rotor field generating elements are disregarded to simplify the characterization of the losses generated).
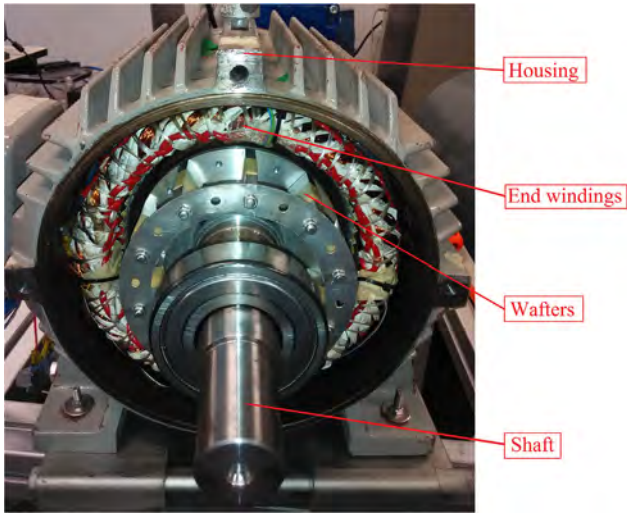


**Fig. 1.** Experimentally tested machine without end-plates.

Because a very detailed geometry could lead to very time-consuming simulations, some simplifications have been made. The most important simplifications are described below.

### 2.1.1. Housing
The housing of this machine was built with axial fins all around the machine to enhance heat transfer to the ambient air (Fig. 1). Modelling these fins would increase the number of elements in the mesh, so instead an equivalent housing (Fig. 2) with a corrected convection heat transfer coefficient was modelled using the formulation from [22].

### 2.1.2. Stator end windings
The machine modelled was built with wound windings, which is the most common topology for traction machines [23], although bar windings could be analysed in the same way. In representing the winding, modelling each of the wires in the winding would lead to very large meshes, so the approximation proposed by Mellor [24] was adopted (Fig. 2).

### 2.1.3. Periodicity and symmetry
In order to reduce the number of cells in the CFD model and thus the computational time required, the following simplifications were included:

- Symmetry: Symmetry with respect to the central vertical plane was assumed in order to model half of the machine on this axis (Fig. 3).
- Periodicity: The least common multiple between the number of wafters and the number of slots was modelled on the circumferential axis (Fig. 3).
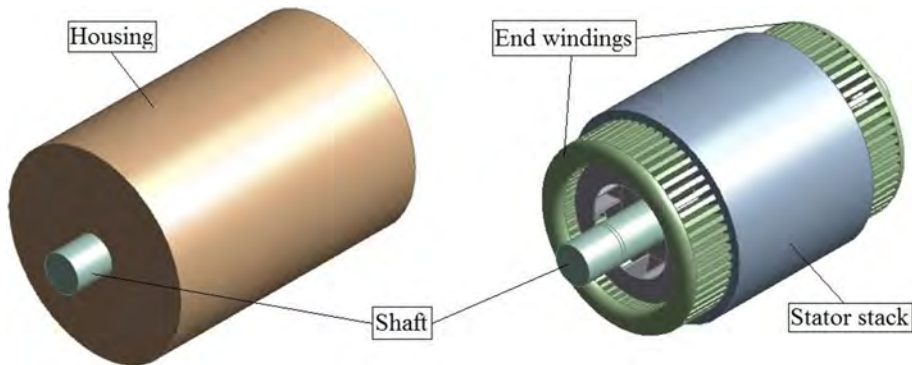


**Fig. 2.** Geometry of the housing (left) and the active parts (right) in the CFD model.
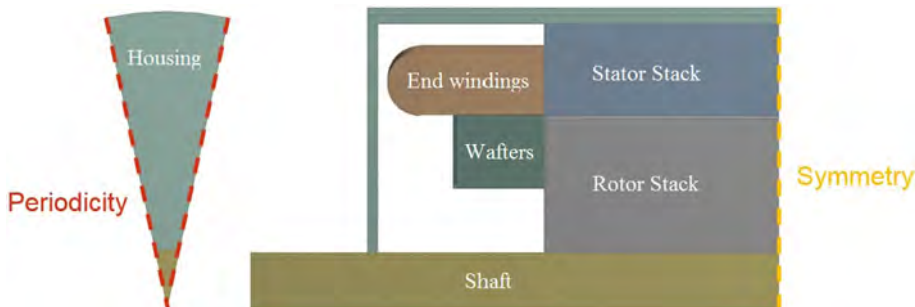


**Fig. 3.** Simplifications made to the model: Circumferential periodicity (left); Central plane symmetry (right).

## 2.2. Mathematical model

The temperatures and the heat transfer coefficients in this electric motor can be studied by solving the governing differential equations that are restricted to the boundary conditions inside the flow domain.

### 2.2.1. Flow domain

The computational flow domain consists mainly of the air inside and the solids that make up the electric motor (the housing, the end-plate, the shaft, the rotor and the stator).

As stated above, simplifications were made to the model's geometry in order to reduce the number of elements in the model. First, a central vertical plane symmetry was imposed in order to model half of the machine. Then, a periodicity of the least common multiple between the number of wafters and the number of stator slots was considered. The reduced model and the whole model (without symmetry or periodicity) were compared, and the same results were obtained. Thus, the reduced model was validated.

A high quality tetrahedral mesh was used to discretize the computational domain. The number of cells was on the order of $1.5 \cdot 10^6$. The resolution of the mesh was higher in the fluid zone, and inflation for the surfaces of the fluid in contact with the solids was included (consisting of a 10-layer grid where y+ < 5), which is a standard in these kind of simulations. In this regard, the different solids were computed using a conformal grid type. However, a non-conformal grid was employed for the contact between the fluid and the solids. Furthermore, skewness and orthogonal quality standards were far below what is recommended by software developers.

### 2.2.2. Governing equations

Analytical estimations of the Re number were made beforehand in order to know the most suitable flow regime. These estimations indicate the existence of a turbulent regime of the flow in the zone where the wafters rotate, and subsequent simulations confirmed the validity of this supposition. Taking the above into account, the unsteady Reynolds averaged Navier-Stokes (URANS) (Eqs. (1) and (2)) and the Energy (Eq. (3)) equations were used to include turbulence effects in the mean flow variables. Density and thermal conductivity were considered constant (Table 1).

$$\frac{\partial \rho}{\partial t} + \frac{\partial}{\partial x_j}(\rho \cdot U_j) = 0 \tag{1}$$

$$\frac{\partial \rho U_i}{\partial t} + \frac{\partial}{\partial x_j}(\rho \cdot U_i \cdot U_j) = -\frac{\partial p}{\partial x_i} + \frac{\partial}{\partial x_j}(\tau_{ij} - \rho \cdot \overline{u_i \cdot u_j}) + S_M \tag{2}$$

$$\frac{\partial \rho h_{hot}}{\partial t} - \frac{\partial p}{\partial t} + \frac{\partial}{\partial x_j}(\rho \cdot U_j \cdot h_{tot}) = \frac{\partial}{\partial x_j}\left(\lambda \frac{\partial T}{\partial x_j} - \rho \overline{u_j \cdot h_{tot}}\right)$$
$$+ \frac{\partial}{\partial x_j}[U_i \cdot (\tau_{ij} - \rho \cdot \overline{u_i \cdot u_j})] + S_E \tag{3}$$

where $\rho$ represents the density of the fluid, t the time, $x_j$ the displacement in j direction, $U_j$ the instantaneous velocity in j direction, p the pressure of the fluid, $\tau_{ij}$ the molecular stress tensor, $h_{tot}$ the mean total enthalpy, T the temperature of the fluid and, $S_M$ and $S_E$ represent source terms of the momentum (Eq. (2)) and the energy (Eq. (3)) equations, respectively.

A great deal of research has been done in the field of CFD simulations for electrical machines, and most of it shows very good agreement with experimental measurements when using the standard k-$\varepsilon$ model. SanAndres [25] developed a CFD design methodology for electric machine cooling systems, Klomberg [26] presented different methods for analysing a large hydro generator with CFD, Dang [27] studied the rotor–stator interaction through CFD simulations, and Melka [28] introduced a validated numerical model describing heat transfer and air flow phenomena in a permanent magnet brushless direct current motor. For this study, the standard k-$\varepsilon$ model was also selected for the turbulence model. In addition, a two-layer approach and the one-equation model by Wolfstein [29], which dealt with turbulence modelling near the walls, were adopted.

### 2.2.3. Boundary conditions

The flow and thermal boundary conditions needed for the complete setup of the model consist of the material database, specified in Table 1, and a list of boundary conditions, defined in Table 2.

For the studied machine, the tip speed (also known as the peripheral speed, which is the theoretical maximum speed of the air due to the movement of the rotating parts of the electrical machine) is always under 0.3 Mach. Consequently, the internal

**Table 1**
Material properties in the CFD model.

| Name | T. conductivity (W/m K) | $C_p$ (J/kg K) | Density (kg/m$^3$) | Zone |
|---|---|---|---|---|
| Air | 0.0242 | 1006.43 | 1.067 | Internal air |
| Insulation | 0.13 | – | – | Contact Stator-winding |
| Varnish | 0.4 | – | – | Contact Winding-air |
| GG20 | 46 | 460 | 7200 | Housing and end-plates |
| F125 | 40.6 | 470 | 7810 | Shaft |
| M600-50A | 36/36/2.75 | 486 | 7750 | Rotor and stator stack |
| Copper | 387.6 | 381 | 8978 | Windings |

**Table 2**
Flow and thermal boundary conditions.

| Zone | Type of boundary condition | Value | Units |
|---|---|---|---|
| Contact Stator-winding | Width of the thermal resistance | 1.7 | mm |
| Contact Winding-air | Width of the thermal resistance | 0.1 | mm |
| Joule losses | Volumetric loss (15/20 A) | 68707.0/122145.7 | W/m$^3$ |
| Bearing losses | Volumetric loss (1000/1750 rpm) | 1770760.2/2810996.0 | W/m$^3$ |
| Rotational speed | Air rotation | 1000/1750 | rpm |
| Ambient | Temperature | 23.4 | °C |
| Turbulence initialization | Turbulence kinetic energy (k) | 1 | m$^2$/s$^2$ |
| Turbulence initialization | Turbulent dissipation ($\varepsilon$) | 1 | m$^2$/s$^3$ |
| Housing external surface | Convection | 25 | W/m$^2$ K |
| End-plate external surface | Convection | 5 | W/m$^2$ K |

air has been considered incompressible and has been modelled with constant density (Table 1).

As Table 2 shows, the copper (Cu) winding of the machine is isolated from the stator stack with insulation material, which is represented with a thermal resistance of 76.5 K/W. In addition, losses in the copper winding are represented with Joule losses, which vary depending on the DC current circulating in the conductors, and mechanical losses in the bearings are taken into account. Furthermore, the ambient temperature and the convective heat transfer coefficient of the external surfaces of the machine are defined in this step. In addition, the following conditions are assumed:

- A no slip condition is assumed for the surface contacts between fluids and solids, where the fluid is supposed to have the same speed as the wall. In addition, smooth walls for the shear stress calculation are assumed for the turbulence model.
- For the symmetry surfaces: the expected pattern of the flow/ thermal solution has mirror symmetry.
- For the periodic surfaces: the flow entering the computational model through one periodic surface is identical to the flow exiting the domain through the opposite periodic surface.
- For the inlet: a turbulent intensity of 5% and a turbulent viscosity ratio of 10 is established.
- For the outlet: a backflow turbulent intensity of 5% and a backflow turbulent viscosity ratio of 10 is assumed, which are default values from the commercial software Ansys FLUENT [30].

Finally, the rotational speed of the rotating elements is also set.

### 2.2.4. Discretization and resolution

The finite volume method (FVM) was applied to discretize the differential equations of the mathematical model described above, using a segregated implicit solver to solve the generated algebraic equation system. Equations were linearized and then sequentially solved using the Gauss-Seidel algorithm accelerated by an algebraic multigrid method [31]. The pressure-velocity coupling was achieved through the use of the SIMPLE algorithm [32]. Diffusive terms of the equations were discretized using a second-order scheme, and the convective terms were discretized using a second-order upwind scheme [33].

As the validation process was performed with transient simulations, a study of the time stepping was performed, and the correct time step was obtained for the following simulations.

The mathematical model was solved on an HP server with 4 Opteron 880 processors and with 16 GB of RAM memory. The entire numerical procedure was implemented in the unstructured CFD code Fluent v16.2 [30].

### 2.2.5. Convergence criteria

Three criteria determine whether convergence is achieved. The first consists in a decrease of three orders of magnitude from the values for the scaled residuals of the equations, maintaining values below $10^{-3}$ for the mass, momentum and turbulent equations and $10^{-6}$ for the energy equation. The second that the mean air temperature must be held constant through iterations. And the third criterion establishes the balance between the energy losses and the energy dissipated through the external surfaces by convection and radiation.

### 2.2.6. Grid independency

The grid independency of the mathematical model results was checked by means of the grid convergence index (GCI), based on the Richardson Extrapolation method [34]. This value is used to determine the discretization error by comparing the results for three different meshes. The first mesh ($N_1$: 5,273,745 elements)

is the finest, the second mesh ($N_2$: 3,208,293) represents an intermediate grid level and the third mesh ($N_3$: 1,100,866) is for a coarse mesh. The resulting refinement factors are $r_{21} = 1.18$ and $r_{32} = 1.428$.

Four results from the model's simulations were selected in order to evaluate the discretization error: mean temperatures in the rotor and the stator windings, and convection with air in the rotor end and the stator end windings. The results of the evaluation are presented in Table 3. These results show that the assumed discretization error is low enough if the fine or intermediate meshes, $N_1$ or $N_2$, are chosen for the mathematical model. In this case, the intermediate mesh was selected in order to minimize computational cost and reduce simulation time.

## 3. Experimental measurements and validation of the CFD model

The validation of the CFD model presented above was carried out by taking certain experimental measurements. These tests were performed under different working conditions, with and without wafters and for different rotation speeds.

### 3.1. Tested machine

As noted above, the machine used in these tests consists of a totally enclosed electric machine with an outer stator and an inner rotor without magnets or copper bars. Thus, rotor field generating elements are disregarded to simplify the characterization of the losses generated (Fig. 4) and the only loss source is located in the stator windings and the bearings.

The main properties of the machine are:

- Rotor external diameter is 162 mm.
- Stator external diameter is 235 mm.
- 60 stator slots.
- Stator stack length is 150 mm.
- End winding axial length is 33 mm.

### 3.2. Test conditions

An induction motor drove the test machine at a constant speed for each of the experiments (Fig. 5). In addition, a torque transducer was placed between the induction motor and the test machine in order to measure the mechanical losses produced by the bearings.

At the same time, the stator windings were supplied with DC current in order to avoid magnetic field variations in the stator stack. Thus, only Joule and mechanic losses are taken into account. The machine was supplied with DC current as shown in Fig. 6 for all configurations.

Losses in the windings ($P_{CuS}$) were obtained experimentally by measuring the resistance of each of the three phases, using Eq. (4).

$$P_{Cu.S} = \frac{1}{\frac{1}{R_{uu}} + \frac{1}{R_{vv}} + \frac{1}{R_{ww}}} \cdot I^2 \qquad (4)$$

where I is the supplied current in Amps and $R_{xx}$ is the resistance in Ohms for phase $xx$ (representing phases $uu$, $vv$ and $ww$) of the machine.

The mechanical losses were obtained experimentally by testing the machine without any loss source and making it rotate at a constant speed of 1000 rpm, measuring the generated torque with the torque transducer.

Six different configurations were analysed. Due to mechanical limitations, only two rotation speeds were studied (1000 and 1750 rpm). For each of these rotation speeds, three different topologies were examined: the motor without wafters, with 30

**Table 3**
Grid independency analysis for the three meshes.

| | | Stator winding temperature (K) | Rotor stack temperature (K) | Convection with air in the end windings (W/m² K) | Convection with air in the rotor end (W/m² K) |
|---|---|---|---|---|---|
| Variable values | $\phi_1$ | 401.31 | 391.7 | 0.91717 | −0.4692 |
| | $\phi_2$ | 401.37 | 391.49 | 0.88856 | −0.47972 |
| | $\phi_3$ | 401.35 | 398.2 | 0.94638 | −0.05134 |
| Absolute differences | $\alpha_{21}$ | 0.06 | −0.21 | −0.02861 | −0.01052 |
| | $\alpha_{32}$ | −0.02 | 6.71 | 0.05782 | 0.42838 |
| Grid convergence index (%) | GCI$_{21}$ | 0.03 | 0.00 | 0.04 | 0.57 |
| | GCI$_{32}$ | 0.00 | 0.00 | 0.00 | 2.45 |
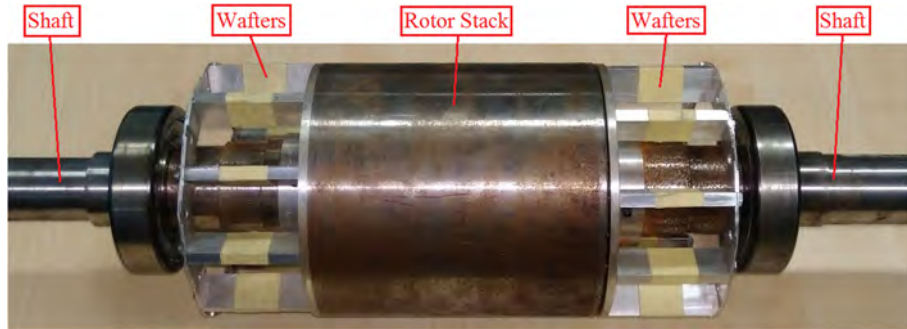


**Fig. 4.** Rotor tested (with no magnets or bars) with wafters.
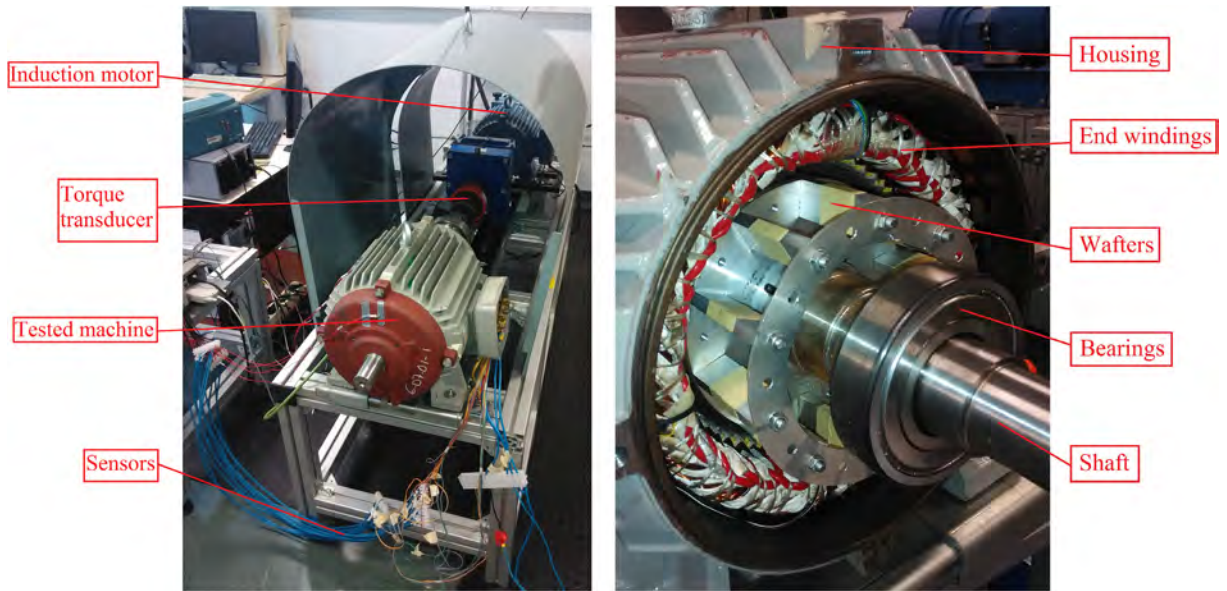


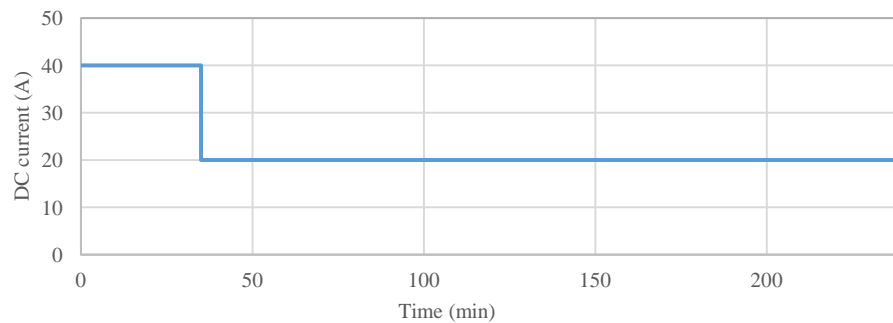**Fig. 5.** Configuration of the tests performed (left) and test machine with 60 mm wafters (right).



**Fig. 6.** Supplied current for the test configurations.

mm axial length wafters and with 60 mm axial length wafters (in the cases with wafters, 10 wafters were placed in both the rotor drive-end (DE) and non-drive-end (NDE), with a height of 20 mm and a width of 7 mm),

The objective of these tests was to measure temperatures in different parts of the machine, focusing mainly on the stator windings, which is the focus of this study. Therefore, fifteen PT-100 temperature sensors were installed in the machine, twelve of which were placed in the stator windings (four in the DE end windings, another four in the NDE end windings and the last four in the middle of the stator stack), two were placed in the housing of the machine, and one was left in the ambient environment.

### 3.3. Results and validation

The results obtained from the temperature measurements were compared with the CFD transient simulations under the same working conditions.

Fig. 7 shows the mean temperature in the end windings of the machine both for experimental tests and CFD simulations. In these graphs, the results of the CFD are represented with the mean surface temperature of the end winding (in orange). In contrast, the experimental results are displayed with the DE and NDE end winding curves, in blue and grey, respectively, which are defined as the mean temperature of each of the 4 sensors located in each of the end windings.

As can be seen, CFD simulations show very good agreement with the experimental data. However, due to some uncertainty with mechanical losses at higher rotational speeds, some disagreement is found in the b, d and f graphs from Fig. 7. Because these mechanical losses are not the focus of study in this article, the deviation was assumed admissible.

Looking at Fig. 7, it can be observed that the reduction in temperatures for tests with 1000 rpm rotation speed is negligible. However, there is a reduction in the maximum temperature by more than 10 °C for the tests with wafters at 1750 rpm. Moreover, the variation in the wafter length (graphs d and f) does not yield a significant reduction in the temperatures of the winding. In addition, the maximum temperature obtained in the tests is shown and compared with the CFD results in Table 4.
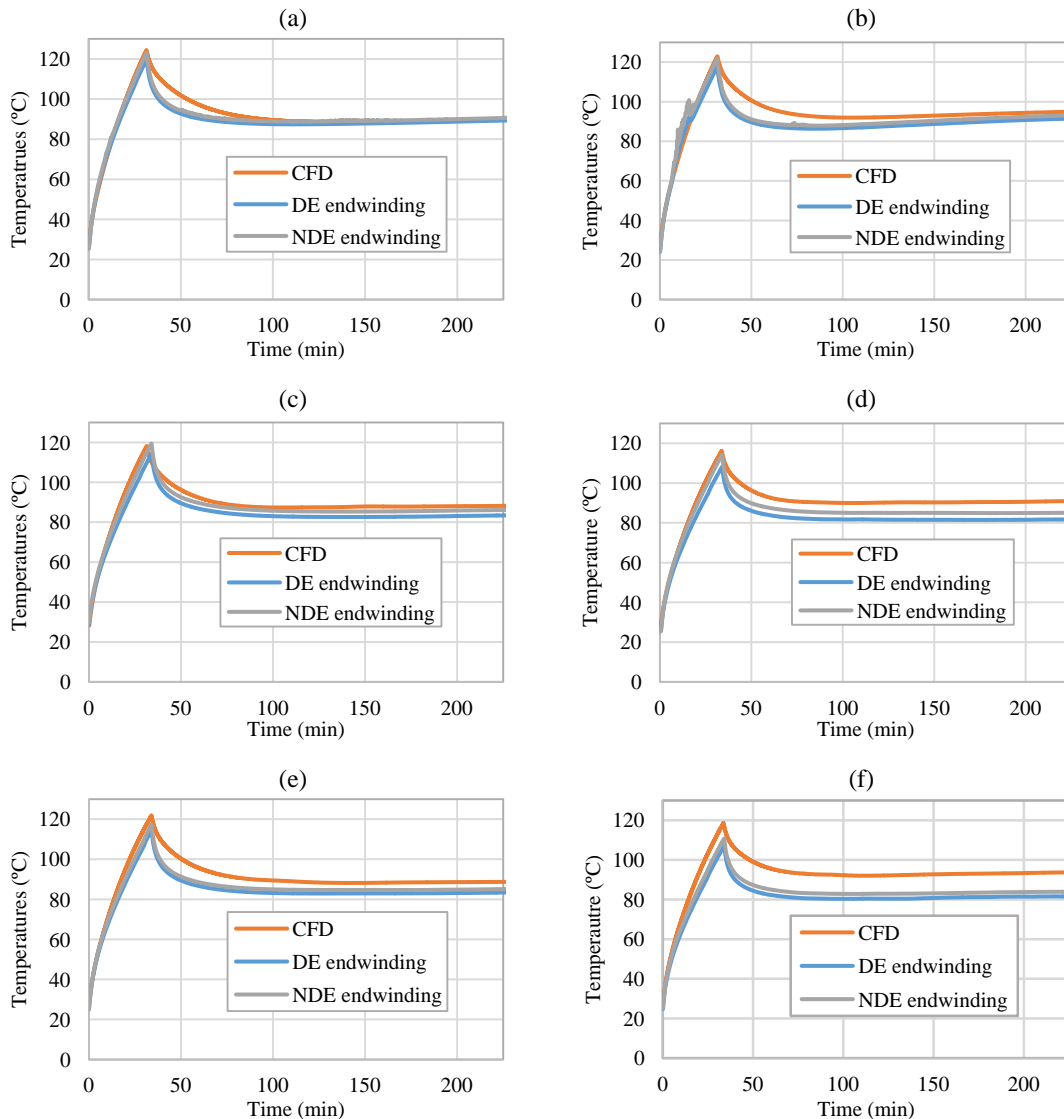


Fig. 7. Comparison of CFD and experimental measurements: (a) 1000 rpm without wafters; (b) 1750 rpm without wafters; (c) 1000 rpm with 30 mm wafters; (d) 1750 rpm with 30 mm wafters; (e) 1000 rpm with 60 mm wafters; (f) 1750 rpm with 60 mm wafters.

**Table 4**
Maximum temperature (in °C) values obtained for each test and CFD simulation.

| Topology | CFD result | Test result | Difference (%) |
|---|---|---|---|
| a | 124.4 | 123.0 | 1.42 |
| b | 122.9 | 121.7 | 1.23 |
| c | 118.2 | 119.4 | −1.26 |
| d | 116.2 | 114.2 | 2.23 |
| e | 121.8 | 117.4 | 4.74 |
| f | 118.53 | 110.9 | 8.83 |

## 4. CFD parametric study

Having validated the CFD model experimentally, we turn to the main objective of this study, which is to identify the effect of different variables on the convective heat transfer coefficient in the end windings, which tend to be the hotspot in many designs. These variables consist of different parameters defining the wafters. Moreover, the additional mechanical losses generated by these wafters are also examined.

### 4.1. Type of study

Three different parametric analyses were performed, each one with different aims, as listed below:

- Parametric Analysis 1: End region without wafters: The model is analysed without wafters. The main purpose of this study is to obtain the convective heat transfer coefficients in the end region without wafters.
- Parametric Analysis 2: End region with wafters (unshrouded): The model with wafters is analysed. The influence of wafters without a shroud in the convective heat transfer coefficients is examined.
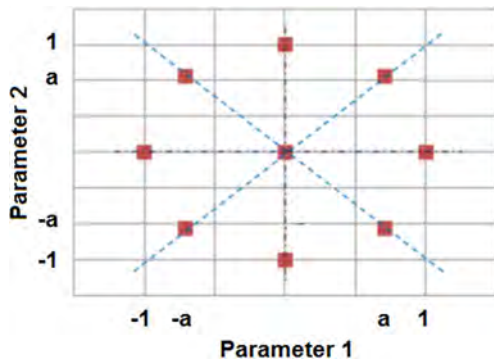


Fig. 8. Example of a CCD with two input parameters where f = 0.

- Parametric Analysis 3: End region with wafters (shrouded): The model with wafters is studied, but this time a shroud for the wafters is included. The influence of the shroud is examined.

For each parametric analysis the same DoE, a central composite design (CCD), was employed. The CCD designs are five-level fractional factorial designs that are suitable for calibrating a quadratic response model. An example of a two-parameter CCD is shown in Fig. 8.

As can be seen in Fig. 8, a CCD consists of:

- A centre point.
- 2·n axis points located at the −a and +a positions (0 < a < 1) on each axis of the selected input material.
- $2^{(n-f)}$ factorial points located at the −1 and +1 positions along the diagonal of the input parameter space.

f is the factorial, which is used to restrict the number of design points to a reasonable number (some diagonal points are not included based on factorial f).

### 4.2. Parameters under study

There are many parameters that could be classified as input parameters in this study, but it would lead to too many design points. Consequently, some parameters were discarded before the DoE was conducted.

#### 4.2.1. Discarded parameters

As the focus of this study is the end region of the machine, parameters such as the number of slots, the geometry of the slot and the airgap were left out of the study. Furthermore, the stator external diameter and the stator stack were defined relative to the rotor external diameter, which is one of the input parameters defined in the nomenclature section. The relation between these parameters was fixed with representative values for traction applications [23], which are commonly designed with 2, 3 or 4 pair poles, and they are listed below:

- Stator stack length ($ls_{tack-Stator}$) and rotor external diameter → $ls_{tack-Stator} = 1.2 * D_{Ext-Rotor}$
- Stator external diameter ($D_{Ext-Stator}$) and rotor external diameter → $D_{Ext-Stator} = 1.5 * D_{Ext-Rotor}$

The wafter width ($b_{wafter}$), which is described in Fig. 9, is always limited by the manufacturing process. As this variable increases, the hydraulic resistance of the end region will also increase,
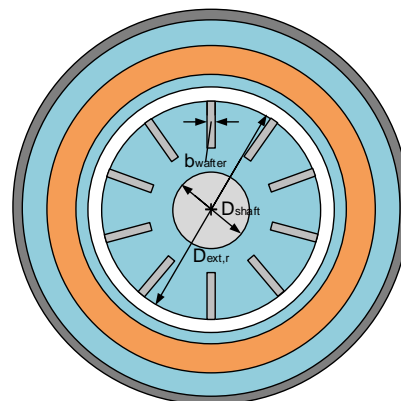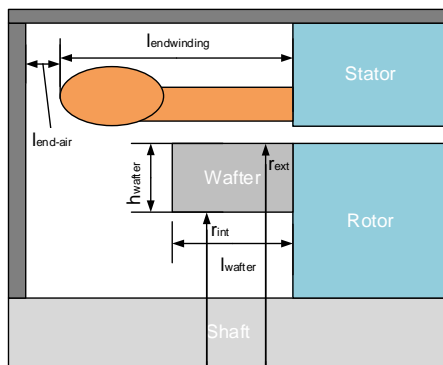


Fig. 9. Parameters under study in the machine.

thereby reducing the air flow in this region. For this reason, this parameter should be kept as low as possible in order to ensure that no mechanical problems occur, such as wafter bending or rupture.

The number of wafters ($z_{wafters}$) was defined with Eq. (5) from [35], which offers a reasonable value for an early stage design. Unfortunately, there is no mathematical method for determining an optimum number of blades/wafters for this case. Care must be exercised in the design of the wafter passages to ensure a reasonable flow of the streamlines such that no separation occurs.

$$z_{wafters} = \frac{8.5}{1 - r_{int}/r_{ext}} \tag{5}$$

where $r_{int}$ and $r_{ext}$ represent the internal and external radius of the wafters, respectively (see Fig. 9). The increase in this parameter leads to higher hydraulic efficiency, but it also increases the amount of mechanical losses in the machine. Although Eq. (5) brings a practical solution to this problem, a deeper study is still recommended for final designs.

The shaft diameter ($D_{shaft}$) was defined according to its mechanical loadability, which is described in [36].

In addition, the distance between the end windings and the plate ($l_{end-air}$ in Fig. 9) was defined by the nominal voltage of the machine (V), and Eq. (6) from [37,38] set this parameter in meters.

$$l_{end-air} = 0.005 \cdot V \tag{6}$$

Finally, the temperature in the windings was set according to the most common insulation class for traction applications in electric motors [39,40]. Consequently, the temperature in the windings was kept constant at 150 °C.

### 4.2.2. Input parameters

The following five input parameters were selected to perform the DoE:

- Speed rotation (rpm), with an upper value of 6000 and a lower value of 1000. These limits were defined using [41] as a reference, setting the range for traction applications from 1000 to 6000 rpm. These rotation speed limits cover a range from small starters to train/bus electric motors.
- Rotor external diameter (m), with a maximum value of 0.35 m and a minimum value of 0.1 m. The main restriction for this variable consisted of limiting the tip speed [42] to under 0.3 Mach for a maximum speed of 6000 rpm. Otherwise, air would not be considered incompressible and CFD simulations would become much more complicated.
- End winding length (m). The length of the end windings was fixed between 0.05 and 0.15 m. These values correspond to feasible values according to the previously defined parameters and the type of application studied. The aim of this limitation is to embrace most of the configurations described for traction applications in the literature.
- Wafter length (m) was limited with variable $X_{wl}$ from Eq. (7), with a maximum value of 1 and a minimum value of 0.3. This way, the optimum wafter length is related to the end winding length.

$$l_{wafter} = X_{wl} \cdot l_{endwinding} \tag{7}$$

- Wafter height (m) was limited with variable $X_{wh}$ from Eq. (8), with a maximum value of 0.8 and a minimum value of 0.2. This way, the optimum value of $h_{wafter}$ is related to the rotor's external diameter and shaft diameter.

$$h_{wafter} = X_{wh} \cdot 0.5 \cdot (D_{Ext-Rotor} - D_{Shaft}) \tag{8}$$

### 4.2.3. Output parameters

Two output parameters were identified in this study:

- Convective heat transfer coefficient in the end windings ($h_{endwinding}$): This parameter is measured in W/m² K and consists of the heat transfer capacity from the end windings to the air inside the machine. As this value grows, the temperatures in the end windings are reduced and a better temperature distribution in the stator winding is obtained, which is the main goal of this study.
- Friction losses inside the machine ($P_{ventilation}$): Measured in Watts (W), ventilation losses inside the machine are obtained with this value. As this value grows, the overall efficiency of the machine is reduced. Consequently, care should be taken with this parameter.

## 5. Results of the parametric study

The data generated from the different DoE was analysed using the commercial software Minitab 17 [43]. The results are presented in two sections. First, the results obtained without wafters are explained, followed by the effects of different parameters for the wafers. These equations are statistical relations where the constants obtained in each equation give the consistency between both terms.

### 5.1. Without wafters

The data obtained in the previous sections was used to develop second-order statistical models, one for each of the variables analysed. The degree of accuracy of these models was determined by the coefficient of determination ($R^2$), which ranges from 0 to 1. For these models, $R^2$s of 0.99 and 0.95 were obtained for the convective heat transfer coefficient and the ventilation losses, respectively. Both models are defined in Eqs. (9) and (10) for the convective heat transfer coefficient ($h_{endwinding}$) and the ventilation losses ($P_{ventilation}$), respectively, where $D_{rotorext}$ and $l_{endwinding}$ are given in meters and N is given in rpm.

$$\begin{aligned} h_{endwinding} = {} & 2.61 + 0.0349 \cdot D_{rotorext} - 0.095 \cdot l_{endwinding} \\ & + 0.0059 \cdot N + 0.000021 \cdot D_{rotorext}^2 \\ & + 0.000961 \cdot l_{endwinding}^2 - 0.00046 \cdot D_{rotorext} \cdot l_{endwinding} \\ & + 0.000019 \cdot D_{rotorext} \cdot N - 0.000042 \cdot l_{endwinding} \cdot N \end{aligned} \tag{9}$$

$$\begin{aligned} P_{ventilation} = {} & 761 - 4.81 \cdot D_{rotorext} - 3.01 \cdot l_{endwinding} - 0.1939 \cdot N \\ & + 0.008 \cdot D_{rotorext}^2 + 0.0151 \cdot l_{endwinding}^2 \\ & + 0.000013 \cdot N^2 - 0.00005 \cdot D_{rotorext} \cdot l_{endwinding} \\ & + 0.000747 \cdot D_{rotorext} \cdot N - 0.000002 \cdot l_{endwinding} \cdot N \end{aligned} \tag{10}$$

As expected, both parameters grew as the rotational speed and the rotor external diameter increased. The convective heat transfer coefficient did not acquire values above 40 W/m² K for any configuration. In addition, ventilation losses were always below 0.65 kW.

### 5.2. With wafters

As mentioned in the previous section, the results shown are based on second-order statistical models. Each of the models was characterized by the coefficient of determination ($R^2$), which were 0.97 and 0.98 for the convective heat transfer coefficient and the ventilation losses, respectively. The second-order models are defined in Eqs. (11) and (12) for the unshrouded case.

$$
\begin{aligned}
h_{endwinding} = {}& -434 + 0.824 \cdot D_{rotorext} - 0.7 \cdot l_{endwinding} + 609 \cdot X_{wl} \\
& + 632 \cdot X_{wh} + 0.0611 \cdot N - 0.001112 \cdot D_{rotorext}^2 \\
& - 0.0037 \cdot l_{endwinding}^2 - 363.5 \cdot X_{wl}^2 - 430.7 \cdot X_{wh}^2 \\
& - 0.000001 \cdot N^2 + 0.00096 \cdot D_{rotorext} \cdot l_{endwinding} \\
& - 0.417 \cdot D_{rotorext} \cdot X_{wl} - 0.196 \cdot D_{rotorext} \cdot X_{wh} \\
& + 0.000038 \cdot D_{rotorext} \cdot N + 1.12 \cdot l_{endwinding} \cdot X_{wl} \\
& + 0.62 \cdot l_{endwinding} \cdot X_{wh} + 0.000238 \cdot l_{endwinding} \cdot N \\
& - 145 \cdot X_{wl} \cdot X_{wh} - 0.0586 \cdot X_{wl} \cdot N - 0.0438 \cdot X_{wh} \cdot N
\end{aligned}
\tag{11}
$$

$$
\begin{aligned}
P_{ventilation} = {}& 10552 - 80.7 \cdot D_{rotorext} - 45.4 \cdot l_{endwinding} + 9231 \cdot X_{wl} \\
& + 4180 \cdot X_{wh} - 3.393 \cdot N + 0.1229 \cdot D_{rotorext}^2 \\
& - 0.0072 \cdot l_{endwinding}^2 - 1670 \cdot X_{wl}^2 - 2884 \cdot X_{wh}^2 \\
& + 0.000207 \cdot N^2 + 0.2218 \cdot D_{rotorext} \cdot l_{endwinding} \\
& - 27.4 \cdot D_{rotorext} \cdot X_{wl} - 3.9 \cdot D_{rotorext} \cdot X_{wh} \\
& + 0.01162 \cdot D_{rotorext} \cdot N - 10.5 \cdot l_{endwinding} \cdot X_{wl} \\
& - 48.0 \cdot l_{endwinding} \cdot X_{wh} + 0.012 \cdot l_{endwinding} \cdot N \\
& + 8462 \cdot X_{wl} \cdot X_{wh} - 1.567 \cdot X_{wl} \cdot N - 0.369 \cdot X_{wh} \cdot N
\end{aligned}
\tag{12}
$$

For the case with shrouded wafters, the second-order models are defined in Eqs. (13) and (14).

$$
\begin{aligned}
h_{endwinding} = {}& -434 + 0.824 \cdot D_{rotorext} - 0.7 \cdot l_{endwinding} + 609 \cdot X_{wl} \\
& + 632 \cdot X_{wh} + 0.0611 \cdot N - 0.001112 \cdot D_{rotorext}^2 \\
& - 0.0037 \cdot l_{endwinding}^2 - 363.5 \cdot X_{wl}^2 - 430.7 \cdot X_{wh}^2 \\
& - 0.000001 \cdot N^2 + 0.00096 \cdot D_{rotorext} \cdot l_{endwinding} \\
& - 0.417 \cdot D_{rotorext} \cdot X_{wl} - 0.196 \cdot D_{rotorext} \cdot X_{wh} \\
& + 0.000038 \cdot D_{rotorext} \cdot N + 1.12 \cdot l_{endwinding} \cdot X_{wl} \\
& + 0.62 \cdot l_{endwinding} \cdot X_{wh} + 0.000238 \cdot l_{endwinding} \cdot N \\
& - 145 \cdot X_{wl} \cdot X_{wh} - 0.0586 \cdot X_{wl} \cdot N - 0.0438 \cdot X_{wh} \cdot N
\end{aligned}
\tag{13}
$$

$$
\begin{aligned}
P_{ventilation} = {}& 10552 - 80.7 \cdot D_{rotorext} - 45.4 \cdot l_{endwinding} + 9231 \cdot X_{wl} \\
& + 4180 \cdot X_{wh} - 3.393 \cdot N + 0.1229 \cdot D_{rotorext}^2 \\
& - 0.0072 \cdot l_{endwinding}^2 - 1670 \cdot X_{wl}^2 - 2884 \cdot X_{wh}^2 \\
& + 0.000207 \cdot N^2 + 0.2218 \cdot D_{rotorext} \cdot l_{endwinding} \\
& - 27.4 \cdot D_{rotorext} \cdot X_{wl} - 3.9 \cdot D_{rotorext} \cdot X_{wh} \\
& + 0.01162 \cdot D_{rotorext} \cdot N - 10.5 \cdot l_{endwinding} \cdot X_{wl} \\
& - 48.0 \cdot l_{endwinding} \cdot X_{wh} + 0.012 \cdot l_{endwinding} \cdot N \\
& + 8462 \cdot X_{wl} \cdot X_{wh} - 1.567 \cdot X_{wl} \cdot N - 0.369 \cdot X_{wh} \cdot N
\end{aligned}
\tag{14}
$$

Predictably, the convective heat transfer coefficient is affected by the rotor external diameter and the rotational speed in the same way as in the case for no wafters.

In addition, the values of the heat transfer coefficient in the end windings are much higher than those without wafters, and this increase will reduce temperatures in the windings. Although there is a reduction in temperatures, care should be taken with the ventilation losses because they are also higher than the case without wafters, where values of 5.8 kW are obtained.

Moreover, to obtain the optimum wafter configuration, the effect of the geometric parameters on the convective heat transfer coefficient that defines the wafters is in Fig. 10. The same information is obtained for the ventilation losses in Fig. 11.

As can be seen in Fig. 10, the optimum configuration would be a shrouded design with a length that is half of the length of the end windings and half the height available between the shaft and the rotor external diameter. However, care should be taken with the ventilation losses because, as depicted in Fig. 11, the ventilation losses are also strongly affected by the geometry of the wafters.

### 5.3. Design criteria for wafters

The main objective of this study is to obtain some criteria to define the geometry of the wafters in order to minimize the temperatures in one of the most critical parts of electrical machines, the stator end windings. The reduction of temperatures in the end windings is achieved by maximizing the convective heat transfer in this zone. Bearing this in mind, the most relevant criteria obtained from this study for the parameters defining the wafters are summarized below:
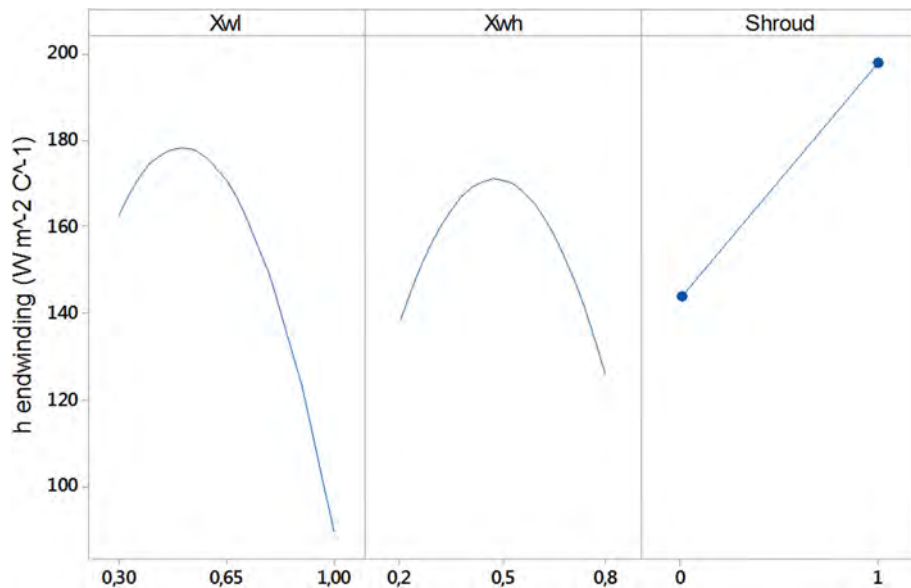


**Fig. 10.** Effects of different geometric parameters that define the wafters on the convective heat transfer coefficient in the end windings.
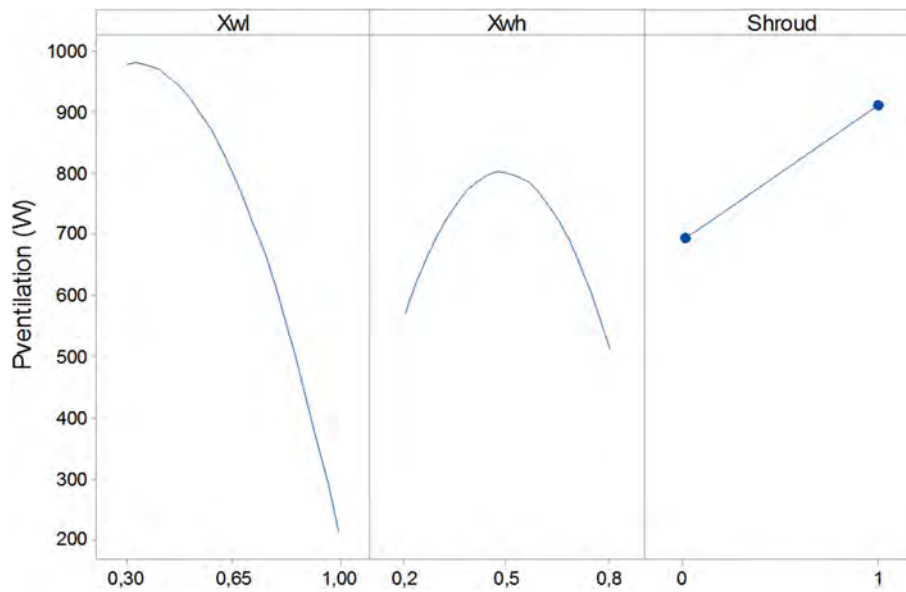
**Fig. 11.** Effects of different geometric parameters that define the wafters on the ventilation losses in the machine.

- The length of wafters ($l_{wafter}$ in Fig. 9): Following the results obtained previously in Fig. 10, the optimum value of $X_{wl}$ to maximize the convective heat transfer coefficient is 0.55. Consequently, the length of the wafters should be around the value obtained from Eq. (15).

$$l_{wafter} = 0.55 \cdot l_{endwinding} \qquad (15)$$

- The height of wafters ($h_{wafter}$ in Fig. 9): Also, with the aim of maximizing the convective heat transfer coefficient (Fig. 10), $X_{wh}$ should be about 0.5. Therefore, the height of wafters should be defined according to Eq. (16).

$$h_{wafter} = 0.25 \cdot (D_{Ext-Rotor} - D_{Shaft}) \qquad (16)$$

- The inclusion of a shroud: The inclusion of this element increases significantly the convective heat transfer in the end windings, as can be seen in Fig. 10. Therefore, its implementation would be beneficial for the thermal behaviour of the machine.
- The wafter width ($b_{wafter}$ in Fig. 9): As commented previously, this parameter is always limited by the manufacturing process. As this variable increases, the hydraulic resistance of the end region will also increase, thereby reducing the air flow in this zone. For this reason, this parameter should be kept as low as possible in order to ensure that no mechanical problems occur.
- The number of wafters ($z_{wafter}$): This parameter has not been analysed in detail in this study, so a deeper analysis should be performed in order to get more insight into the influence of this parameter. In this regard, Eq. (5) from [35] offers a reasonable value for an early stage design.

### 5.4. Example

To check the accuracy of the statistical models developed, apply the developed design criteria and observe the influence of the wafters in a real case, the same machine with and without wafters was examined using the previous CFD models.

#### 5.4.1. Machine characteristics and working conditions

The example machine used in this section is based on a permanent magnet surface mounted (PMSM) machine that can be

**Table 5**
Main characteristics of the machine studied.

| Parameter | Value | Units |
|---|---|---|
| Rotational speed | 3000 | rpm |
| Nominal power | 46.44 | kW |
| Rotor external diameter | 200 | mm |
| Stator stack length | 240 | mm |
| Stator external diameter | 300 | mm |
| Number of slots | 60 | – |
| End winding length | 80 | mm |
| Airgap | 2 | mm |

employed for traction applications. Common values for speed rotation, nominal power and machine size were obtained from Burress [23]. In addition, recommended values from [36] were obtained to develop the rest of the geometry. The resulting machine is described in Table 5.

In addition, the design criteria obtained in Section 5.3 was employed in order to define the geometry of the wafters, yielding:

- 30 wafters (15 for NDE and 15 for DE).
- 44.36 mm length in the axial direction.
- 36.06 mm height in the radial direction.
- 3 mm width.
- A shrouded topology (of 2 mm width).

#### 5.4.2. CFD model

The CFD models are not described in detail in this section because the same CFD models used in previous sections were used to conduct the study in this section. The properties of the CFD models are described in Section 2.

The only difference between the current CFD model and the above CFD models is that the temperature in the windings was not fixed this time and losses in the stator stack and windings were included.

#### 5.4.3. Working conditions

To represent the thermal behaviour of the machine with and without wafters, the results obtained in CFD represent the steady state temperatures for nominal conditions.
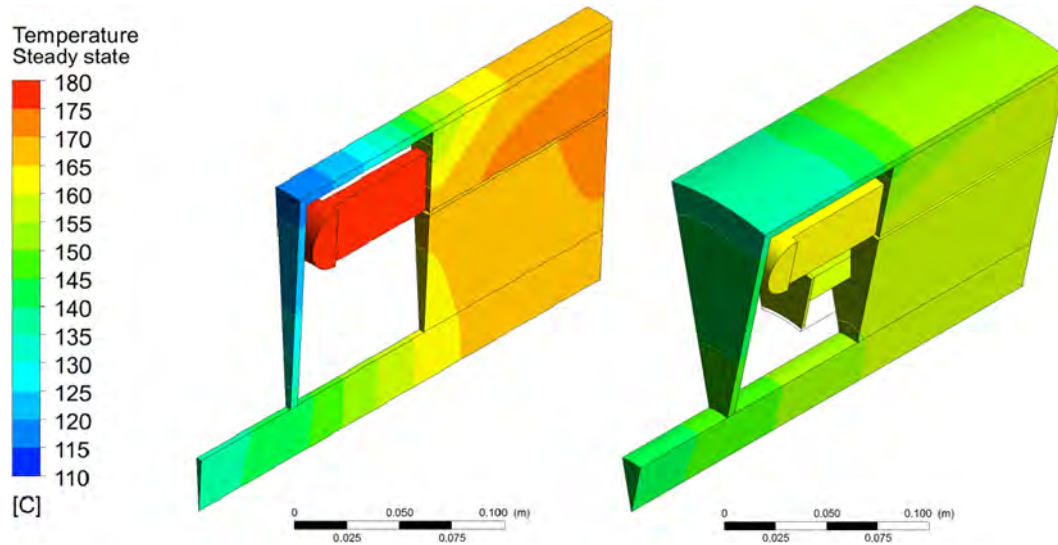
**Fig. 12.** Steady state temperatures for the model without wafters (left) and the model with wafters (right).

Therefore, the losses were obtained from the nominal power of the machine, assuming 1.95% of the nominal power for the winding losses and 1.05% for the losses in the stator stack (which are common values for PMSM for a traction application). In this regard, the working conditions are listed below:

- A rotational speed of 3000 rpm.
- An ambient temperature of 25 °C.
- 864 W of losses in the stator winding.
- 486 W of losses in the stator stack.

### 5.4.4. Thermal behaviour without wafters

The values obtained for the convective heat transfer coefficient in the end windings in the statistical model (18.41 W/m$^2$ K) and in the CFD (19.13 W/m$^2$ K) are in acceptable agreement (difference of 3.79%), which could be very useful for analytical thermal models of this kind of topology.

The steady state thermal behaviour of the machine is shown in Fig. 12, where a maximum temperature of 178.1 °C was found in the end windings of the machine.

### 5.4.5. Thermal behaviour with wafters

As occurred in the previous section, the values obtained for the convective heat transfer coefficient in the end windings in the statistical model (165.69 W/m$^2$ K) and the CFD (152.25 W/m$^2$ K) showed good agreement (difference of 8.83%), which could be also employed for the analytical modelling of this element.

In addition, temperatures decreased by 16.2 °C in the end windings, obtaining a hotspot of 161.9 °C, as seen in Fig. 12.

Although this is significant reduction, two phenomena that could affect this comparison are not included in the study and are described below:

- For the same output torque, the extra ventilation losses generated due to the wafters' rotation will produce a slight increase in the current of the windings for the case without wafters. Consequently, the winding losses will be slightly higher in the case with wafters, thus increasing the temperature.
- The electric resistivity of the windings is temperature-dependent. Consequently, the case with wafters will suffer a reduction in the winding losses since the windings are colder than the case without wafters. Therefore, the temperatures in the case with wafters may be even lower.

For this comparison, the effect of both phenomena is considered to cancel each other out. However, this should be examined in final stage designs.

## 6. Conclusions

The effect of including wafters in a totally enclosed machine with wound windings was analysed using statistical tools and CFD simulations, and the following conclusions were obtained:

- The inclusion of wafters in a specific machine is translated into a considerable reduction in temperatures and an increase in ventilation losses, which is essential for thermally required designs. For the example given, a reduction of 16.2 °C was obtained.
- Wafter design can be approached using statistical tools such as DoE, where the optimum configuration can be obtained for a limited region. Based on the statistical model obtained, for the particular case of a totally enclosed machine with wound windings, design criteria for minimizing temperatures is obtained.
- Second-order statistical models can accurately determine the convective heat transfer coefficient for a wide range of topologies, which can be very beneficial for modelling analytical thermal models.
- The effect of the number of wafters on the convective heat transfer was not analysed in detail, so a deeper analysis should be performed in order to get better insight into the influence of this parameter.
- Although this paper focuses on wound windings, the methodology could be applied to any kind of windings, such as coil-form windings or hairpin windings, in future research.

## References

[1] Z.Q. Zhu, Y. Chen, Y. Yao, Q. Lu, X. Huang, Y. Ye, Thermal modeling and analysis of double-sided water-cooled permanent magnet linear synchronous machines, COMPEL Int, J. Comput. Math. Electr. Electron. Eng. 35 (2016) 695–712.
[2] C.-B. Park, Thermal Analysis of IPMSM with Water Cooling Jacket for Railway Vehicles, J. Electr. Eng. Technol. 9 (2014) 882–887.
[3] K.-S. Kim, B.-H. Lee, J.-W. Jung, J.-P. Hong, Thermal analysis of water cooled ISG based on a thermal equivalent circuit network, J. Electr. Eng. Technol. 9 (2014) 742–747.

[4] B. Zhang, R. Qu, J. Wang, W. Xu, X. Fan, Y. Chen, Thermal Model of Totally Enclosed Water-Cooled Permanent-Magnet Synchronous Machines for Electric Vehicle Application, Ind. Appl. IEEE Trans. 51 (2015) 3020–3029.
[5] P. Ponomarev, M. Polikarpova, J. Pyrhönen, Thermal modeling of directly-oil-cooled permanent magnet synchronous machine, in: Electr. Mach. (ICEM), 2012 XXth Int. Conf., IEEE, 2012, pp. 1882–1887.
[6] S. Nategh, Z. Huang, A. Krings, O. Wallmark, M. Leksell, Thermal modeling of directly cooled electric machines using lumped parameter and limited CFD analysis, IEEE Trans. Energy Convers. (2013), https://doi.org/10.1109/TEC.2013.2283089.
[7] Equipmake, APM 120R Electric Vehicle Traction Motor, 2017. http://www.equipmake.co.uk/featured-projects/electric-vehicle-traction-motor.
[8] Porsche, Porsche Panamera E-hybrid, 2017. http://www.porsche.com/uk/models/panamera/panamera-s-e-hybrid/featuresandspecs/.
[9] D.H. Lim, S.C. Kim, Thermal performance of oil spray cooling system for in-wheel motor in electric vehicles, Appl. Therm. Eng. 63 (2014) 577–587.
[10] M. Popescu, D. Staton, A. Boglietti, A. Cavagnino, D. Hawkins, J. Goss, Modern heat extraction systems for electrical machines–a review, in: Electr. Mach. Des. Control Diagnosis (WEMDCD), 2015 IEEE Work., IEEE, 2015, pp. 289–296.
[11] S. Wiak, A. Krawczyk, I. Dolezel, Z. Kolondzovski, Determination of critical thermal operations for high-speed permanent magnet electrical machines, COMPEL Int. J. Comput. Math. Electr. Electron. Eng. 27 (2008) 720–727.
[12] Y. Chen, W. Chen, J. Zhou, Y. Fang, Y. Yao, Multi-field Coupled Analysis of a Permanent Magnet Synchronous Motor: Application to High Speed Rail Traction (2016).
[13] M. Polikarpova, P. Lindh, C. Gerada, M. Rilla, V. Naumanen, J. Pyrhönen, Thermal effects of stator potting in an axial-flux permanent magnet synchronous generator, Appl. Therm. Eng. 75 (2015) 421–429.
[14] C. Micallef, End Winding Cooling in Electric Machines, University of Nottingham, 2006.
[15] L. Fedoseyev, E.M. Pearce, Rotor Assembly with Heat Pipe Cooling System (2016).
[16] C. Tighe, C. Gerada, S. Pickering, Assessment of Cooling Methods for Increased Power Density in Electrical Machines (2016).
[17] D. Camilleri, R. Rolston, Rotor Radial Vent Pumping in Large Synchronous Electrical Machines (2016).
[18] C. Micallef, S.J. Pickeringt, K.A. Simmons, K.J. Bradley, An alternative cooling arrangement for the end region of a totally enclosed fan cooled (TEFC) induction motor, in: Power Electron. Mach. Drives, 2008. PEMD 2008. 4th IET Conf., IET, 2008, pp. 305–309.
[19] C. Micallef, S.J. Pickering, K.A. Simmons, K.J. Bradley, Improved cooling in the end region of a strip-wound totally enclosed fan-cooled induction electric machine, IEEE Trans. Ind. Electron. 55 (2008) 3517–3524, https://doi.org/10.1109/TIE.2008.2003101.
[20] A. Athavale, K. Sasaki, B.S. Gagas, T. Kato, R.D. Lorenz, Variable flux permanent magnet synchronous machine (VF-PMSM) design to meet electric vehicle traction requirements with reduced losses, ECCE 2016 - IEEE Energy Convers, Congr. Expo. Proc. 9994 (2017), https://doi.org/10.1109/ECCE.2016.7855549.
[21] M.K. Hussain, P. Gomez, Equivalent Representation of Machine Winding in Frequency Domain Model for Fast Transient Studies (2017).
[22] F.P. Incropera, Fundamentals of Heat and Mass Transfer (2011).
[23] T. Burress, S. Campbell, Benchmarking EV and HEV power electronics and electric machines, in: Transp. Electrif. Conf. Expo (ITEC), 2013 IEEE, IEEE, 2013, pp. 1–6.
[24] P.H. Mellor, D. Roberts, D.R. Turner, Lumped parameter thermal model for electrical machines of TEFC design, Electr. Power Appl. IEE Proc. B. 138 (1991) 205–218.
[25] U. SanAndres, G. Almandoz, J. Poza, G. Ugalde, Design of cooling systems using computational fluid dynamics and analytical thermal models, IEEE Trans. Ind. Electron. 61 (2014) 4383–4391.
[26] S. Klomberg, E. Farnleitner, G. Kastner, O. Biro, Comparison of CFD analyzing strategies for hydro generators, in: Electr. Mach. (ICEM), 2014 Int. Conf., IEEE, 2014, pp. 1995–1995.
[27] D.-D. Dang, X.-T. Pham, Numerical analysis of turbulent convective heat transfer in a rotor-stator configuration, in: Math. Comput. Approaches Adv. Mod. Sci. Eng, Springer, 2016, pp. 413–424.
[28] B. Melka, J. Smolka, Z. Bulinski, A. Ryfa, J. Hetmanczyk, D. Makiela, A validated numerical model of heat and mass transfer in a PM BLDC electric motor, in: 2016 Int. Symp. Power Electron. Electr. Drives, Autom. Motion, IEEE, 2016, pp. 1409–1413.
[29] T. Jongen, Y.P. Marx, Design of an unconditionally stable, positive scheme for the K-ε and two-layer turbulence models, Comput. Fluids. 26 (1997) 469–487.
[30] Ansys, FLUENT, 2015. http://www.ansys.com/.
[31] B.R. Hutchinson, G.D. Raithby, A multigrid method based on the additive correction strategy, Numer. Heat Transf. Part A Appl. 9 (1986) 511–537.
[32] S. Patankar, Numerical heat transfer and fluid flow, CRC Press, 1980.
[33] S.R. Mathur, J.Y. Murthy, A pressure-based method for unstructured meshes, Numer. Heat Transf. 31 (1997) 195–215.
[34] P.J. Roache, Perspective: a method for uniform reporting of grid refinement studies, J. Fluids Eng. 116 (1994) 405–413.
[35] B. Eck, Fans (1974).
[36] J. Pyrhönen, T. Jokinen, V. Hrabovcová, H. Niemelä, Design of Rotating Electrical Machines (2008).
[37] J.C. Martín, Cálculo industrial de máquinas eléctricas – Tomo I (1982).
[38] J.C. Martín, Calculo Industrial De Maquinas Electricas – Tomo II (1982).
[39] B. Sarlioglu, C.T. Morris, D. Han, S. Li, Driving Toward Accessibility (2016), https://doi.org/10.1109/MIAS.2016.2600739.
[40] S.C. Kim, Thermal performance of motor and inverter in an integrated starter generator system for a hybrid electric vehicle, Energies (2013), https://doi.org/10.3390/en6116102.
[41] A.M. El-Refaie, Motors/generators for traction/propulsion applications: A review, IEEE Veh. Technol. Mag. 8 (2011) 90–99.
[42] S. Li, Y. Li, W. Choi, B. Sarlioglu, High-Speed Electric Machines: Challenges and Design Considerations, IEEE Trans. Transp. Electrif. 2 (2016) 2–13.
[43] Minitab, Minitab 17, 2017. http://www.minitab.com.